eng

MDPI

Article

One-Dimensional Drift-Flux Modeling of Gas–Liquid Flow in Inclined Gas-Lift Pipelines

Yijie Liu [1,2]

[1] School of Ocean and Civil Engineering, Shanghai Jiao Tong University, Shanghai 200240, China; lyj635417909@gmail.com
[2] Department of Mechanical Engineering, The University of Tokyo, Tokyo 113-8656, Japan

Abstract

Gas-lift performance depends on pipeline inclination and gas injection conditions. This study examines these effects using an unsteady, one-dimensional gas–liquid drift-flux model and a finite-volume solver. The carrier liquid is Newtonian with prescribed density and viscosity; separate solid-particle transport is not modeled. The application cases cover static inclinations of 60–90° from the horizontal, a pipe diameter of 0.1023 m, and an axial length of 197 m. Comparisons with inclined bubble drift and vertical airlift measurements assess different aspects of the formulation. Grid and time step comparisons are reported as sensitivity checks. At a fixed axial injection distance of 185 m below the still-water intersection, the vertical injection depth decreases from 185 m at 90° to 160.21 m at 60°. Thus, the inclination comparison changes both the hydrostatic head and the adopted slip closure. Injection rate comparisons of 0.1–0.4 kg s^{-1} and axial injection distance comparisons of 160–185 m show changes in gas holdup, phase velocities, and start-up behavior. The results describe comparative gas–liquid hydrodynamics within the stated assumptions; they do not establish compressor energy efficiency or validated deep-sea slurry throughput.

Keywords: deep-sea mining; gas-lift system; inclined pipeline; drift-flux model; two-phase flow; numerical simulation

1. Introduction

Gas injection can drive upward transport by reducing the average density of the fluid inside a lifting pipe relative to the surrounding liquid [1,2]. This principle has motivated studies of airlift systems for subsea resource recovery [3,4]. Gas expansion, interphase slip, and wall friction jointly determine the liquid delivery rate and the transient response [5,6]. For deep-sea applications, the carrier-flow problem is also coupled to particle transport and riser mechanics [7–9]. These additional processes must be distinguished from the gas–liquid hydrodynamics considered here: a two-phase flow model alone does not establish the environmental performance or solids recovery capability of a mining system.

Gas lift is an established pumping principle; the novelty sought here concerns its mathematical representation and the interpretation of specified operating cases. Applications extend beyond offshore recovery. Enany et al. [10] investigated mine-water pumping with different injection arrangements and submergence ratios, demonstrating the importance of injector configuration to system performance. Kajishima and Saito [11] developed an unsteady airlift calculation and compared it with a 200 m facility. Together with

Academic Editor: Antonio Gil Bravo

Received: 19 September 2026
Revised: 22 October 2026
Accepted: 30 October 2026
Published: 3 November 2026

Copyright: © 2026 by the author. Licensee MDPI, Basel, Switzerland. This article is an open access article distributed under the terms and conditions of the Creative Commons Attribution (CC BY) license.

the laboratory and pilot-scale measurements of Saito et al. [12], this work provides an experimental and numerical foundation for studying long lifting columns.

Previous airlift studies provide complementary information on fluid properties, flow development, and pumping performance. Kamata and Ito [13] reported that the liquid flow rate was more sensitive to liquid density than to viscosity under their tested conditions. Moisidis and Kastrinakis [14,15] examined flow pattern transitions and pressure behavior in short airlift pumps. Wahba et al. [16] investigated airlift performance using analytical models and large-eddy simulation, while Gao et al. [5] studied bubble motion in lifting pipes. These approaches resolve different spatial and temporal scales. For long risers, a one-dimensional formulation offers a practical way to compare axial pressure, phase transport, and start-up behavior across operating cases. Offshore deployment also motivates consideration of nonvertical configurations, because a supported riser need not remain vertical [17]. Figure 1 illustrates this application context; the present calculations prescribe each inclination and do not solve wave-induced motion.

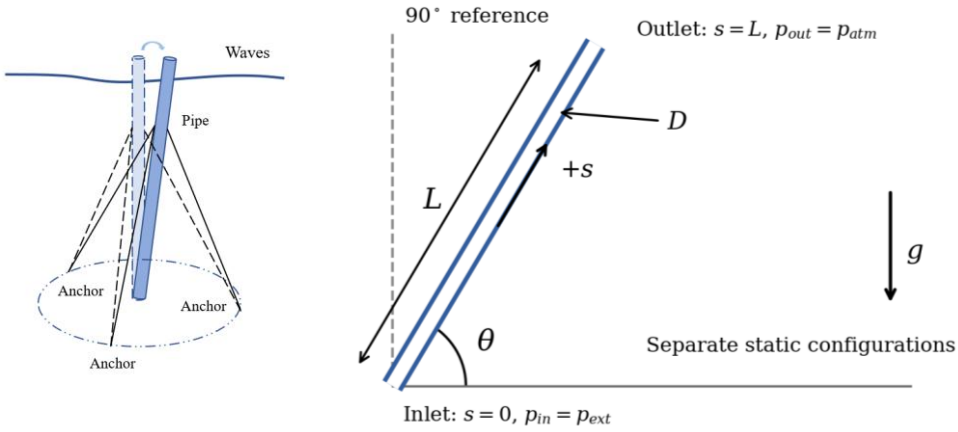


Figure 1. Offshore gas-lift application and prescribed static inclination, with $\theta = 90°$ for a vertical pipe and $60° \leq \theta < 90°$ for the inclined cases, measured from the horizontal. Left: offshore application, in which the solid and dashed lines denote the inclined and vertical pipe positions and their mooring lines to the anchors. Right: pipe-axis definitions, with the arrows indicating the pipe length L, diameter D, positive flow coordinate s and gravity g; the dashed vertical line is the 90° reference.

Inclination changes both the axial component of gravity and the relative motion of gas and liquid. The experiments by Bendiksen [18] and the work on lifting-pipe geometry by Hanafizadeh et al. [6] show why orientation and geometry require explicit treatment. Bhagwat and Ghajar [19,20] developed correlations for gas holdup across different orientations and flow conditions. However, the range of an individual empirical correlation does not automatically become the validated range of a solver that combines it with other closures. In particular, a vertical-pipe friction relation and an inclination-dependent drift relation require joint assessment when applied to a long, compressible gas-lift column. The practical question addressed here is how prescribed inclination changes the predicted carrier-flow response when injection rate and injection position are varied.

Inclination and curvature are related but distinct geometric effects. Fujimoto et al. [21] measured changes in particle transport performance caused by local bends, while Kassab et al. [22] examined the hydrodynamics of bent airlift risers. A single inclination angle cannot represent the additional losses and redistribution associated with these configurations. The straight inclined cases considered here isolate orientation-dependent gravity and drift; they provide a reference for subsequent calculations with spatially varying geometry.

Recent work further distinguishes gas–liquid closure development from complete resource transport modeling. Shimizu et al. [23] analyzed hybrid airlift transport of rare-earth-rich mud and polymetallic nodules, and their subsequent study [24] examined unsteady hybrid-lifting operations. Those studies explicitly address material transport processes that are outside a carrier-only model. Hibiki et al. [25] developed a full-range correlation for upward cocurrent flow in vertical pipes, emphasizing the relation between closure construction and validation data. Heydari et al. [26] combined drift-flux modeling with a flow pattern map based on mixture velocity and gas volumetric quality. Together, these developments show why void fraction alone is insufficient for regime identification and why validation of a vertical flow correlation cannot be transferred automatically to inclined slurry transport.

Extending a gas–liquid calculation to drilling fluids, tailings, or mineral mud requires independently characterized rheology and, where particles have appreciable relative motion, explicit solids transport. The present Newtonian calculations address the carrier-flow component of this wider problem.

The present work assembles established drift-flux and wall-friction relations in a one-dimensional finite-volume framework and applies them to a controlled comparison of static inclinations. Its contribution is the combined examination of axial profiles, start-up gas holdup evolution, and gas injection choices for the specified gas–liquid cases. It does not introduce a universally validated drift-flux correlation or a resolved three-phase slurry model. Frictional pressure drop measurements for resource transport systems [27] remain important for extending this scope. The distinction between computational parameter ranges, experimental comparison conditions, and extrapolated application cases is maintained throughout.

The reduced dimensionality makes repeated comparisons over a long axial domain tractable while retaining gas compressibility, separate phase mass fluxes, and algebraic slip. This is the practical advantage of the formulation for examining injection choices and static inclination. It does not resolve cross-sectional vortices, bubble size distributions, individual liquid slugs, or structural deformation, and no computational speed benchmark against three-dimensional simulation is claimed.

The paper is organized as follows. Section 2 presents the one-dimensional governing equations and closure relations, including pipe diameter and inclination effects. Section 3 describes the computational domain and numerical procedure. Section 4 presents numerical sensitivity checks and comparisons with published experiments. Section 5 examines inclination, gas injection rate, and injection location. Section 6 summarizes the findings and the limits of their application.

2. Mathematical Models

The governing equations describe unsteady, one-dimensional, cross-section-averaged gas–liquid flow in a straight pipe. The model resolves axial variation only; it does not resolve individual bubbles, radial segregation, or turbulent eddies. Turbulent transport is represented indirectly through empirical wall-friction and drift-flux closures, rather than a separate turbulence transport model. Their use is restricted by the fluid properties, Reynolds numbers, geometry, and flow conditions for which the closures are appropriate. Deep-sea mining motivates the configuration, but the calculated liquid is a Newtonian carrier rather than a concentration-dependent slurry. The following assumptions define the calculation:

(1) The inclination θ is prescribed and remains constant in each calculation. It is measured from the horizontal, so $\theta = 90°$ denotes a vertical pipe. Application cases use $\theta = 90°$, 80°, 70°, and 60°. Waves and currents motivate these comparisons but are not dynamically coupled to the internal flow.

(2) The pipe is straight with constant circular area A = πD²/4. The upward axial coordinate s runs from the inlet at s = 0 to the outlet at s = L. Let ZH be the axial submerged length and ZL the axial distance from the still-water intersection down to the injection point. Then sinj = ZH − ZL, and the vertical injection depth is hinj = ZL sin θ. With the still-water elevation as zero, h(s) = (s − ZH) sin θ and hout = (L − ZH) sin θ. The axial dimensions are held fixed when inclination is varied. Consequently, vertical submergence and hydrostatic boundary pressures vary with θ; ZL is not itself a vertical depth except at θ = 90°.

(3) The flow is isothermal, without phase change or dissolution. The liquid density and dynamic viscosity are prescribed constants. No solid-phase continuity or momentum equation, solids concentration, settling law, or shear-rate-dependent viscosity is included. The void-fraction intervals used in the closure selection are modeling conventions, not a complete physical flow regime map.

2.1. Governing Equations

The drift-flux formulation combines phase mass conservation, mixture momentum, and algebraic relative-motion closures [28–31]. The gas fraction αg is cross-section averaged. The following bubbly, intermediate, and annular expressions denote limiting closure branches rather than independently identified flow morphologies. Their dimensional drift term is vgj,90 = Uσ v*gj, where Uσ = [gσ(ϱl − ϱg)/ϱl²]¼, lc = [σ/(g(ϱl − ϱg))]½, ND = D/lc, and μ* = μl/(ϱlσlc)½. The density ordering ϱl > ϱg is assumed. Inclination is subsequently applied to the closure drift term through Equation (25). The simulations reported here used this dimensionally consistent form, including the Uσ factor in the annular branch.

Low-void-fraction limiting closure, evaluated at the vertical reference orientation:

$$C_0 = (1.2 - 0.2\sqrt{\frac{\rho_g}{\rho_l}})(1 - e^{-18\alpha_g}) \quad (1)$$

$$v_{gj,90} = 1.41(1 - \alpha_g)^{1.75} U_\sigma \quad (2)$$

Intermediate limiting closure; Equation (4) gives the $\mu^* > 2.25 \times 10^{-3}$ branch:

$$C_0 = 1.2 - 0.2\sqrt{\frac{\rho_g}{\rho_l}} \quad (3)$$

$$v_{gj,90} = 0.92(\frac{\rho_g}{\rho_l})^{-0.157} U_\sigma \quad (4)$$

High-void-fraction limiting closure, with its dimensional velocity scale included:

$$C_0 = 1 + C_A \quad (5)$$

$$v_{gj,90} = U_\sigma C_A \sqrt{\frac{(1 - \alpha_g) N_D}{0.015}} \quad (6)$$

$$C_A = \frac{1 - \alpha_g}{\alpha_g + \sqrt{\frac{\rho_g(1 + 75(1 - \alpha_g))}{\sqrt{\alpha_g}\rho_l}}} \quad (7)$$

The limiting pairs (C0, vgj,90) are interpolated together. The bubbly closure is used for $\alpha g \leq 0.20$; the bubbly and intermediate values are linearly blended over $0.20 < \alpha g < 0.30$ using w = (αg − 0.20)/0.10. The intermediate closure applies over $0.30 \leq \alpha g \leq 0.70$; the

intermediate and annular values are blended over 0.70 < αg < 0.80 using w = (αg − 0.70)/0.10. The annular closure applies for $\alpha g \geq 0.80$. Within a transition, each interpolated quantity is (1 − w) times the lower branch plus w times the upper branch. The values 0.25 and 0.75 are transition midpoints, not universal regime boundaries.

In Equations (1)–(7), C0 is a dimensionless distribution parameter representing the influence of nonuniform phase and velocity profiles on the area-averaged gas flux. The velocity vgj,90 represents the remaining relative-motion contribution at the vertical reference orientation. The scale Uσ combines buoyancy and surface tension and has units of velocity; lc compares capillary and gravitational effects, and ND measures pipe diameter relative to that length. The density ratio, gas fraction, and dimensionless viscosity determine the selected empirical branch. CA in Equations (5)–(7) is the dimensionless auxiliary coefficient of the high-void-fraction closure, not pipe area. These relations close the averaged balances without solving a bubble population or a radial velocity field; their branch names do not constitute independent observations of flow morphology.

$$\frac{\partial \rho_m}{\partial t} + \frac{\partial (\rho_m v_m)}{\partial z} = \Gamma_m \tag{8}$$

$$\frac{\partial (\alpha_g \rho_g)}{\partial t} + \frac{\partial (\alpha_g \rho_g v_g)}{\partial z} = \Gamma_g \tag{9}$$

$$\frac{\partial (\rho_m v_m)}{\partial t} + \frac{\partial (\rho_m v^2{}_m)}{\partial z} = -\frac{dP_m}{dz} - \rho_m g \sin\theta - \frac{4\tau_w}{D} - \frac{\partial}{\partial z}\left(\frac{\alpha_g \rho_g \rho_l}{\alpha_l \rho_m} {V_{Gj}}^2\right) \tag{10}$$

$$v_m = \frac{\alpha_g \rho_g v_g + \alpha_l \rho_l v_l}{\rho_m} \tag{11}$$

$$\rho_m = \alpha_g \rho_g + \alpha_l \rho_l \tag{12}$$

$$\alpha_g + \alpha_l = 1 \tag{13}$$

$$J_m = J_g + J_l \tag{14}$$

$$V_{Gj} = v_g - J_m \tag{15}$$

$$v_g = C_0 J_m + v_{gj,\theta} \tag{16}$$

Subscripts l and g denote liquid and gas. The mass-averaged velocity vm is defined by Equation (11), and the mixture density ϱm by Equation (12). The coordinate z in Equations (8)–(10) denotes the upward pipe-axis coordinate s, and t is time. Gravity has magnitude g > 0, giving the axial acceleration −g sin θ. The external mass sources Γg and Γm have units kg m^{-3} s^{-1}. For gas injection into cell j, Γg,j = Γm,j = ṁg,inj(t)/(AΔsj), while Γl = 0 and all external sources vanish elsewhere. The discrete gas and mixture continuity equations both receive ṁg,inj/A after integration over the axial cell length. Consequently, Σi Γg,i AΔsi = ṁg,inj. The base implementation ramps the injection as ṁg,inj(t) = ṁg,max min(t/tr, 1), with tr = 60 s and backward-Euler time weighting. Gas expansion is represented by density and void-fraction changes, not by gas mass creation. No separate injector-jet momentum is resolved.

Equations (8) and (9) express mixture and gas mass conservation after cross-sectional averaging at each time; they are not steady or time-averaged balances. For phase k, αk is its occupied cross-sectional area divided by A, vk is the intrinsic phase-averaged axial velocity, and Jk = αkvk is the superficial velocity. The single pressure and phase densities are representative section values in this one-dimensional approximation. Equation (10) balances mixture inertia against pressure, axial gravity, wall friction, and the additional

momentum flux associated with relative-phase motion. The mass-averaged velocity vm in Equation (11) differs from the volumetric mixture flux Jm in Equation (14). These distinctions are necessary when interpreting both the convective fluxes and the drift term.

The symbol ΓL, when used for the liquid source, is identical to Γl and is zero in this study. It is a prescribed external mass-source term, not a constitutive equation or an empirical interphase-transfer correlation. There is no liquid injection, phase change, or dissolution in the modeled domain. Gas injection is specified through Γg, and the same added mass enters Γm. Accordingly, Γm = Γg + Γl; gas expansion changes the local volume occupied by a conserved gas mass through the equation of state.

For clarity, Equation (10) is written with −ϱmg sin θ as the gravitational force per unit volume; all other pressure and wall-friction terms use the same upward-axis convention.

The bulk drift difference VGj = vg − Jm and closure drift term vgj,θ in vg = C0Jm + vgj,θ are distinct. After the local equation of state, the branch interpolation, and the inclination correction have been evaluated, the phase velocities are recovered algebraically from the mass-averaged velocity vm. Defining Δϱ = ϱl − ϱg, the following relations close the kinematics:

$$V_{Gj} = \frac{(C_0 - 1)v_m + v_{gj,\theta}}{1 - (C_0 - 1)\dfrac{\alpha_g \Delta\rho}{\rho_m}}$$

$$J_m = v_m + \frac{\alpha_g \Delta\rho}{\rho_m} V_{Gj}, \quad v_g = J_m + V_{Gj}$$

$$v_l = \frac{J_m - \alpha_g v_g}{1 - \alpha_g}, \quad J_k = \alpha_k v_k$$

These relations apply for αg < 1 and a nonzero recovery denominator. At αg = 0, the gas-free limit is Jm = vl = vm and the drift-stress contribution vanishes. With pabs, αg, and vm determined by the coupled balances, the equation of state, branch correlations, wall-friction relation, injection source, and pressure boundaries specify the remaining local quantities. No additional independent slip variable is required.

The dimensionless viscosity is μ* = μl/(ϱlσlc)½. For μ* ≤ 2.25 × 10⁻³, the intermediate drift term in the wide-range routine is $\frac{v_{gj}}{U_\sigma} = 0.0019 N_D{}^{0.809} (\rho g/\rho l)^{-0.157} (\mu *)^{-0.562}$ when ND ≤ 30, and $\frac{v_{gj}}{U_\sigma} = 0.030 (\rho g/\rho l)^{-0.157} (\mu *)^{-0.562}$ when ND > 30. For larger μ*, it reduces to Equation (4). This diameter- and viscosity-dependent branch selection is distinct from the void-fraction interpolation described above.

2.2. Pipe Diameter and Wall-Friction Closures

The dimensionless pipe diameter ND is defined by Equation (17), and the dimensional capillary length lc by Equation (18). The two-phase friction closure follows the large-diameter airlift formulation [31–34]. Its coefficient is denoted by Cf to avoid confusion with pipe area A. The phase contributions Gk are pressure gradients based on superficial velocities Jk = αkvk. Equations (19)–(23) describe upward cocurrent flow. The Darcy factor is evaluated from the Colebrook relation in the branch implemented here; this does not establish validity in the laminar limit. The implementation sets Gf = 0 for Rel < 100 and omits the gas contribution for Reg < 0.1. These low-flow cutoffs are numerical safeguards, not a separate validated laminar-flow correlation.

$$N_D = \frac{D}{l_c} \tag{17}$$

$$l_c = \sqrt{\frac{\sigma}{g(\rho_l - \rho_g)}} \tag{18}$$

$$G_f = \frac{4\tau_w}{D} = G_l + G_g + C_f\sqrt{G_l G_g} \quad (19)$$

$$C_f = 83N_D^{-0.37} \quad (20)$$

$$G_k = \frac{\lambda_k \rho_k J_k |J_k|}{2D}, \quad k = g, l \quad (21)$$

$$Re_k = \frac{\rho_k D |J_k|}{\mu_k}, \quad k = g, l \quad (22)$$

$$\frac{1}{\sqrt{\lambda_k}} = -2\log\left(\frac{\frac{\varepsilon}{D}}{3.71} + \frac{2.51}{Re_k\sqrt{\lambda_k}}\right) \quad k = g, l \quad (23)$$

Surface tension σ has units N m^{-1}, the Darcy factor λk is dimensionless, and ε is absolute roughness in meters. The stored friction quantity is Gf = 4τw/D in Pa m^{-1}. Wall shear stress is τw = DGf/4 in Pa. Thus, a raw Gf output must be converted before it can be plotted as wall shear stress. The quantities are distinguished explicitly in the nomenclature and the momentum equation. The frictional pressure gradient profiles in Section 5 display the stored Gf output directly and are labeled as frictional pressure gradient in Pa/m; the curve values are unchanged.

2.3. Inclination Correction and Its Scope

Inclination-dependent drift-flux correlations have been discussed by Bhagwat and Ghajar [20]. Here the adopted multiplicative correction in Equation (25) is specified for upward flow, with 60° ≤ θ ≤ 90° in the application cases. It modifies the closure drift term vgj,90, rather than redefining the identity VGj = vg − Jm. Equation (24) defines a dimensionless reference drift Froude number using the dimensional diameter D; it is not a downward-flow switching criterion. This combined closure is the modeling choice assessed here and is not presented as the complete Bhagwat–Ghajar correlation or as a validated horizontal/downward-flow model.

$$Fr_{gj} = \frac{v_{gj,90}}{\sqrt{gD\frac{\rho_l - \rho_g}{\rho_l}}} \quad (24)$$

For the liquid viscosity used here, μl/μref = 1.3 with μref = 1.0 × 10^{-3} Pa s, and the selected viscosity factor is C1 = 1. The sign factor is C2 = 1 throughout the upward application range. The unused downward-flow condition has been removed. The multiplier fθ = (sin θ)½(1 + cos θ)^1.2 equals unity at 90°. Gravity in the mixture momentum equation remains −ϱmg sin θ; the slip correction and the axial gravity projection play different roles.

$$v_{gj,\theta} = v_{gj,90}\sqrt{\sin\theta}(1 + \cos\theta)^{1.2}C_1C_2 \quad (25)$$

$$C_1 = 1, \quad \frac{\mu_l}{\mu_{ref}} = 1.3 \quad (26)$$

$$C_2 = 1, \quad 60° \le \theta \le 90° \quad (27)$$

3. Numerical Model

3.1. Calculation Configurations

The one-dimensional C++ finite-volume solver advances the Newtonian gas–liquid model. Figure 2 identifies the pressure boundaries, localized injection source, and staggered variable locations. The full submerged pipe or a domain beginning at the injection point can be represented. In the latter configuration, the liquid-only segment below injection enters through its hydrostatic head and friction loss. Table 1 lists the reported manuscript inputs; the parameter bounds describe solver inputs rather than validated operating ranges.

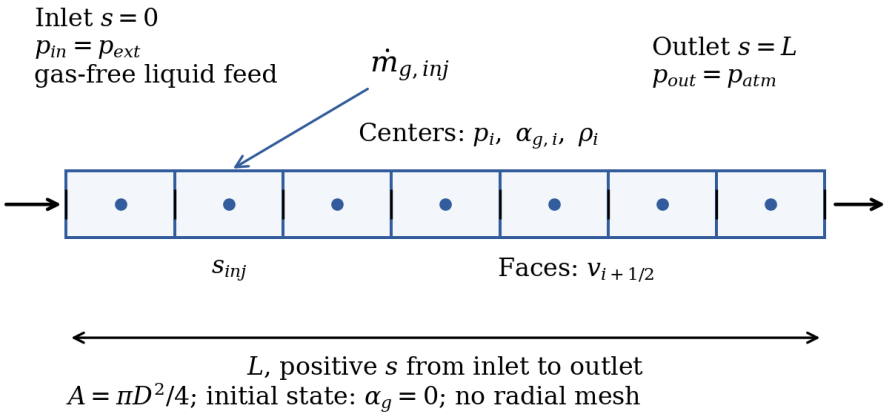


Figure 2. One-dimensional pipe-axis domain with inlet and outlet pressure boundaries, localized gas injection, and staggered scalar and velocity locations.

Table 1. Prescribed fluid properties and computational setup; parameter limits are not validated operating ranges.

Gas	Parameter	Value
	Density	ϱg = pabs/(RaT)
	Viscosity	1.76×10^{-5} Pa s
Liquid		
	Density	1.02×10^{3} kg m^{-3}
	Viscosity	1.3×10^{-3} Pa s
Inlet		
	Pressure inlet	$P_{liquid-static} + P_{atm}$
	Void fraction	$\alpha_{\text{initial,in}} = 0$
	Pressure corrector	$\delta P_{in} = 0$
	Injected phase (gas) flow rate	0–100 kg/s
Outlet		
	Pressure outlet	P_{atm}
	Initial void fraction	$\alpha_{\text{initial,out}} = 0$
	Pressure corrector	$\delta P_{out} = 0$
Pipe		
	Diameter	0 < D ≤ 1 m
	Inclination	90–60°
	Total length	0 < L ≤ 5000 m

Gas density is evaluated from absolute pressure using ϱg = pabs/(RaT), with Ra = 287 J kg^{-1} K^{-1} and T = 293.15 K. The prescribed Newtonian liquid properties are ϱl = 1.02×10^{3} kg m^{-3} and μl = 1.3×10^{-3} Pa s. Surface tension is σ = 0.0728 N m^{-1} and the base smooth-wall setting is ε/D = 0. For the full pipe, pin = patm + ϱlgZH sin θ. If the domain starts at

injection, $p_{inj} = p_{atm} + \varrho_l g Z_L \sin\theta - \Delta p_{f,below}$, where $\Delta p_{f,below}$ is the liquid-only friction loss below injection. The outlet relation is $p_{out} = p_{atm} \exp[-g_{hout}/(R_a T)]$, approximately atmospheric for the small discharge elevation. The initial pipe and liquid inlet are gas-free. During discharge, $\alpha_{g,out} = 1.5\alpha_{g,N} - 0.5\alpha_{g,N-1}$. The implemented bound $0 \le \alpha_g \le 0.9$ is a numerical safeguard, not a flow pattern criterion or proof of exact conservation.

The injector is represented as a localized, prescribed gas mass source with the 60 s ramp defined in Section 2.1. Its port diameter, hole arrangement, jet breakup, feed-line pressure loss, and compressor control are not resolved. Physically, the gas supply pressure at injection must exceed the local mixture pressure by the pressure loss required to pass the specified flow through the injector and supply line. This requirement constrains realizable operation but is not a calculated hardware limit in the present mass flow-controlled model. Injector-specific measurements or a calibrated pressure–flow relation would be required to couple supply pressure to the delivered gas rate.

The prescribed outlet pressure represents discharge to an ambient-pressure receiver. Gas expansion and evolving mixture density within the pipe remain in the unsteady balances, but the downstream separator, gas plenum, throttling element, and discharge-jet reaction are not part of the domain. Their pressure feedback can change holdup, delivery, and transient loads, particularly during intermittent discharge. A coupled receiver pressure or outlet impedance model would be required for that assessment. The present results therefore describe internal carrier-flow response under the stated pressure boundary and do not quantify resolved slug impacts or discharge-induced structural loads.

3.2. Calculation Scheme

The equations are discretized on a one-dimensional staggered finite-volume grid, with pressure, density, and void fraction at cell centers and axial velocity at faces. A SIMPLER iteration updates material properties and drift, assembles the momentum equation, obtains pressure and velocity corrections, and solves gas continuity. Tridiagonal systems are solved by TDMA. QUICK interpolation with deferred correction is applied to spatial convection. The time-weighting parameter is denoted by ϑ to distinguish it from inclination θ; $\vartheta = 1$ in the base implementation gives backward-Euler time discretization. Underrelaxation is applied between unsuccessful coupled iterations. Equations (28)–(37) and Appendix A summarize the algebraic treatment.

The implemented stopping test compares the sums of absolute successive changes in void fraction and mixture velocity with a common numerical threshold of 10^{-3} in the code units. Pressure changes are calculated but are not included in this stopping test. The test is therefore an unnormalized iteration-change criterion, not a normalized conservation-residual criterion. The initial pressure, velocity, and void-fraction relaxation factors are 0.1, 0.1, and 0.025, with a 400-iteration limit. After liquid outflow begins, these become 0.025, 0.025, and 0.005, with a 3000-iteration limit. Reaching an iteration limit alone does not demonstrate convergence. These implementation settings must be distinguished from the grid and time step series reported in Figure 3.

https://doi.org/10.3390/eng7110607

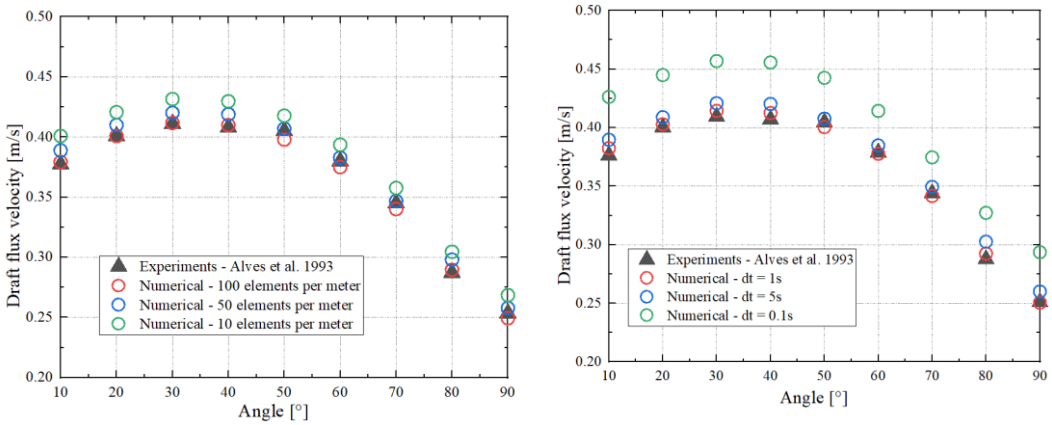


Figure 3. Drift velocity sensitivity to axial grid spacing (**left**) and time step (**right**), compared with the experiments by Alves et al. [35].

The finite-volume method (FVM) integrates each balance over an axial control volume and couples neighboring volumes through shared face fluxes. This supports local conservation when the coupled algebraic balances are converged. The staggered arrangement links face momentum to cell pressure and avoids an independent collocated pressure mode. SIMPLER denotes the Semi-Implicit Method for Pressure-Linked Equations Revised and provides the pressure–velocity coupling; TDMA denotes the tridiagonal matrix algorithm used for the resulting one-dimensional linear systems. Neither method by itself establishes nonlinear convergence or discretization independence.

QUICK denotes Quadratic Upstream Interpolation for Convective Kinematics. Its upstream-biased quadratic face reconstruction reduces the diffusion of first-order upwinding in smooth regions; on a uniform grid the face interpolation is formally third-order. Deferred correction retains an upwind contribution in the implicit matrix and evaluates the higher-order correction from a lagged state. The reconstruction is not inherently bounded near steep gradients, and under-relaxation and void-fraction limits do not constitute a proof of monotonicity or exact conservation. Backward Euler is first-order accurate in time and damps rapid transients. These properties motivate the separate spatial and temporal sensitivity checks in Section 4.1.

3.3. Discretization of Mathematical Model

In Equations (28)–(37), i denotes a spatial index, N the terminal spatial index, and superscripts n and n + 1 the known and updated time levels. Half-indices denote the interlaced scalar or velocity locations shown in Figure 2; Δs and Δt are the axial spacing and time step. The generic transported quantity is ϕ. The signed selector β determines the interpolation direction through max(β, 0) and max(−β, 0). Aw, Ap, Ae, and Aee are reconstruction weights for the displayed upstream and downstream stencil; they are unrelated to pipe area A. Si is the explicitly evaluated, lagged interpolation correction. In the conservation equations, Smce and Sgce denote the collected right-hand-side terms of the mixture and gas balances, including prescribed sources as applicable; they are not additional closure laws. Subscripts g, l, and m identify gas, liquid, and mixture quantities. The weight ϑ denotes time discretization, whereas θ denotes inclination.

The scalar and velocity control volumes are staggered along the pipe axis. The main grid interpolation is written in the following form:

$$\phi_i^{n+1} = max[\beta_i, 0]\phi_{i-1}^{n+1} + max[-\beta_i, 0]\phi_i^{n+1} + S_i^n \quad (28)$$

$$S_i^n = A_w\phi_{i-2}^n + A_p\phi_{i-1}^n + A_e\phi_i^n + A_{ee}\phi_{i+1}^n \quad (29)$$

The corresponding staggered-grid interpolation is

$$\phi_i^{n+1} = max[\beta_i, 0]\phi_i^{n+1} + max[-\beta_i, 0]\phi_{i+1}^{n+1} + S_i^n \tag{30}$$

$$S_i^n = A_w\phi_{i-1}^n + A_p\phi_i^n + A_e\phi_{i+1}^n + A_{ee}\phi_{i+2}^n \tag{31}$$

The reported boundary discretization is

$$(\rho_m v_m)_{N+1/2}^{n+1} = (\rho_m v_m)_{N+1/2}^n - \frac{\Delta t}{\Delta s}\begin{Bmatrix}(v_g)_{N+1/2}^{n+1}\left[(\alpha_g\rho_g)_{N+1}^{n+1}(v_g)_{N+1}^{n+1} - (\alpha_g\rho_g)_N^{n+1}(v_g)_N^{n+1}\right] \\ +(v_l)_{N+1/2}^{n+1}[(\alpha_l\rho_l)_{N+1}^{n+1}(v_l)_{N+1}^{n+1} - (\alpha_l\rho_l)_N^{n+1}(v_l)_N^{n+1}]\end{Bmatrix} \tag{32}$$

$$(\alpha_g\rho_g)_N^{n+1} = (\alpha_g\rho_g)_N^n - \frac{\Delta t}{\Delta s}(v_g)_N^{n+1}\left[(\alpha_g\rho_g)_{N+1/2}^{n+1} - (\alpha_g\rho_g)_{N-1/2}^{n+1}\right] \tag{33}$$

$$(\alpha_l)_N^{n+1} = (\alpha_l)_N^n - \frac{\Delta t}{\Delta s}(v_l)_N^{n+1}\left[(\alpha_l)_{N+1/2}^{n+1} - (\alpha_l)_{N-1/2}^{n+1}\right] \tag{34}$$

The reported discrete conservation equations are listed below; Appendix A provides the associated boundary and momentum algebra.

$$[(\rho_m)_{N-1}^{n+1} - (\rho_m)_{N-1}^n]\cdot\frac{\Delta s}{\Delta t} + \vartheta[(\rho_m)_N^{n+1}(v_m)_N^{n+1} - (\rho_m)_{N-1}^{n+1}(v_m)_{N-1}^{n+1}] = (S_{mce})_{N-1}^n \tag{35}$$

$$(\alpha_g)_{N-1}^{n+1} = max[\beta, 0](\alpha_g)_{N-2}^{n+1} + max[-\beta, 0](\alpha_g)_{N-1}^{n+1} + S_{N-1}^n \tag{36}$$

$$\frac{\Delta s}{\Delta t}(\alpha_g)_{N-1}^{n+1}(\rho_g)_{N-1}^{n+1} + \vartheta\left[(\alpha_g)_N^{n+1}(\rho_g)_N^{n+1}(v_g)_N^{n+1} - (\alpha_g)_{N-1}^{n+1}(\rho_g)_{N-1}^{n+1}(v_g)_{N-1}^{n+1}\right] = (S_{gce})_{N-1}^n + \frac{\Delta s}{\Delta t}(\alpha_g)_{N-1}^n(\rho_g)_{N-1}^n \tag{37}$$

4. Evaluation

4.1. Grid and Time Step Sensitivity

Figure 3 compares drift-velocity predictions with the inclined-pipe measurements of Alves et al. [35]. The legend gives 10, 50, and 100 control volumes per meter, corresponding to $\Delta s = 0.1$, 0.02, and 0.01 m. The total cell count is $N = L/\Delta s$ and depends on the computational length. The reported intermediate settings are 50 control volumes per meter and $\Delta t = 1$ s. The staggered grid contains cell-centered scalars and face velocities; the cell count remains fixed while spacing is updated during the initial rise in the internal liquid level. A default example input is not a substitute for the figure-specific settings.

The reported grids are uniform in the axial direction at each stage; no adaptive refinement or three-dimensional radial mesh is used. The localized source is distributed over its receiving control volume and normalized by that cell volume, so changing Δs does not change the prescribed total injected mass rate. This normalization does not remove spatial error near injection. The injector region, the advancing gas-rich front, and the discharge boundary require particular attention because gradients can be steep there. The present study uses global axial-spacing comparisons rather than locally refined patches; local refinement and common-time transient comparisons would be needed to quantify errors in those regions beyond the sensitivity evidence reported here.

The right-hand panel compares $\Delta t = 0.1$, 1, and 5 s. The 0.1 s predictions are systematically higher, while the 1 and 5 s curves lie closer together. This is a time step sensitivity result and does not demonstrate temporal independence. Backward Euler damps an oscillatory mode according to $|G| = [1 + (\omega\Delta t)^2] - ½$, so increasing the step suppresses transient fluctuations more strongly. This mechanism is consistent with the known temporal diffusion of implicit pipe-flow calculations [36], but it does not by itself identify the cause of the present differences. The temporal term vanishes in a fully converged steady balance; persistent differences must also be examined against common physical sampling times, nonlinear convergence, and time-dependent flow behavior. Agreement with experiment

at Δt = 1 s can include compensating model and discretization errors. No asymptotic convergence rate or uncertainty bound is inferred from Figure 3.

4.2. Verification and Validation

Figure 4 compares liquid mass flow predictions with seven vertical airlift experimental series [12,37–39] (Table 2), while Figure 3 addresses inclined bubble drift. For experimental values y_i and predictions $\hat{y}_i$ paired at equal gas mass flow rates, the relative deviation is $r_i = \frac{\hat{y}_i - y_i}{y_i}$. The mean absolute and signed relative deviations are $\text{MARD} = \frac{100}{N}\sum_{i=1}^{N}|r_i|$ and $\text{MRD} = \frac{100}{N}\sum_{i=1}^{N} r_i$, respectively, expressed as percentages; positive MRD denotes overprediction. Across N = 68 equally weighted pairs, MARD = 5.94% and MRD = +0.02%. Of these, 56 (82.35%) lie within ±10%, and all lie within ±20%; the maximum absolute relative deviation is 18.95%. The Usami series shows systematic underprediction (MARD = 13.59%, MRD = −13.59%); the other six series have MARD values of 2.89–6.27%. The small pooled MRD reflects the balance of positive and negative deviations, resolved by series in Table 2. Local entrance, exit, or injector losses are distinct from distributed friction; no fitted component loss coefficients are claimed here.

Table 2. Dataset identifiers and liquid mass flow prediction errors for the experimental series in Figure 4.

ID	Series in Figure 4	Ref.	N	MARD (%)	MRD (%)
W1	Weber 1976-a	[37]	5	3.89	+3.89
W2	Weber 1976-b	[37]	3	5.22	+5.22
U1	Usami 1982	[38]	10	13.59	−13.59
S1	Saito 1991-a	[39]	10	6.27	+6.27
S2	Saito 1991-b	[39]	16	2.89	+0.02
S3	Saito 2004-a	[12]	11	4.36	−1.04
S4	Saito 2004-b	[12]	13	5.83	+3.89
All	Seven series	[12,37–39]	68	5.94	+0.02

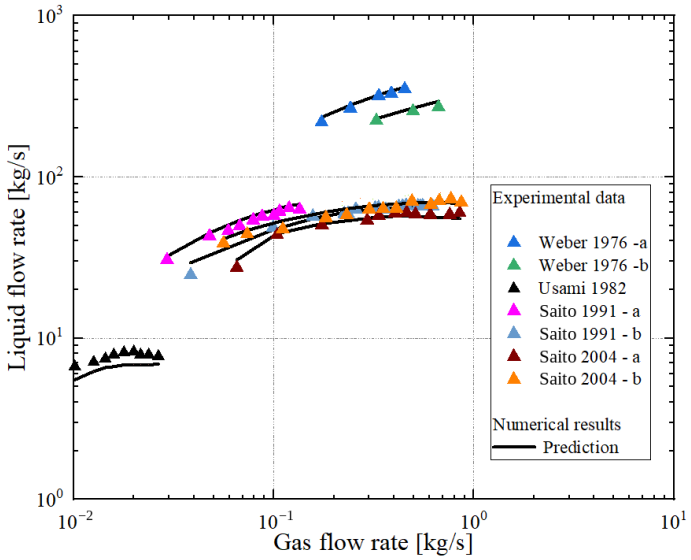


Figure 4. Comparison of calculated and experimental liquid mass flow rates for the vertical airlift datasets [12,37–39].

The validation evidence concerns specific gas–liquid observables and should be interpreted accordingly. The source study of Saito et al. [12] reports laboratory and pilot-

scale facilities spanning pipe diameters of 47–151 mm and heights of 7.7–196.6 m; thus the underlying literature is not limited to short laboratory tubes. These are the ranges reported by that source, not a claim that the 68 paired points in Figure 4 cover every combination. Agreement in vertical liquid throughput and inclined bubble drift supports these tested quantities, but does not validate an inclined, particle-laden deep-ocean riser. Extrapolation also depends on L/D, submergence, ND, phase Reynolds numbers, density ratio, and absolute-pressure range. Gas expansion is included through the isothermal ideal-gas relation; real-gas behavior, heat transfer, dissolution, solids loading, and changing pipe geometry remain outside the present assessment.

5. Results and Discussion

5.1. Simulations of Inclined and Vertical Pipe

The inclination comparison uses θ = 90°, 80°, 70°, and 60°, D = 0.1023 m, L = 197 m, ZL = 185 m, and $\dot{m}_{g,inj}$ = 0.3 kg s^{-1}. ZL is measured along the pipe from the still-water intersection to the injector. Table 3 reports the case conditions and the geometrically determined vertical injection depths. These are illustrative Newtonian gas–liquid cases. Figure 5 presents cross-section-averaged gas fraction against axial position and time.

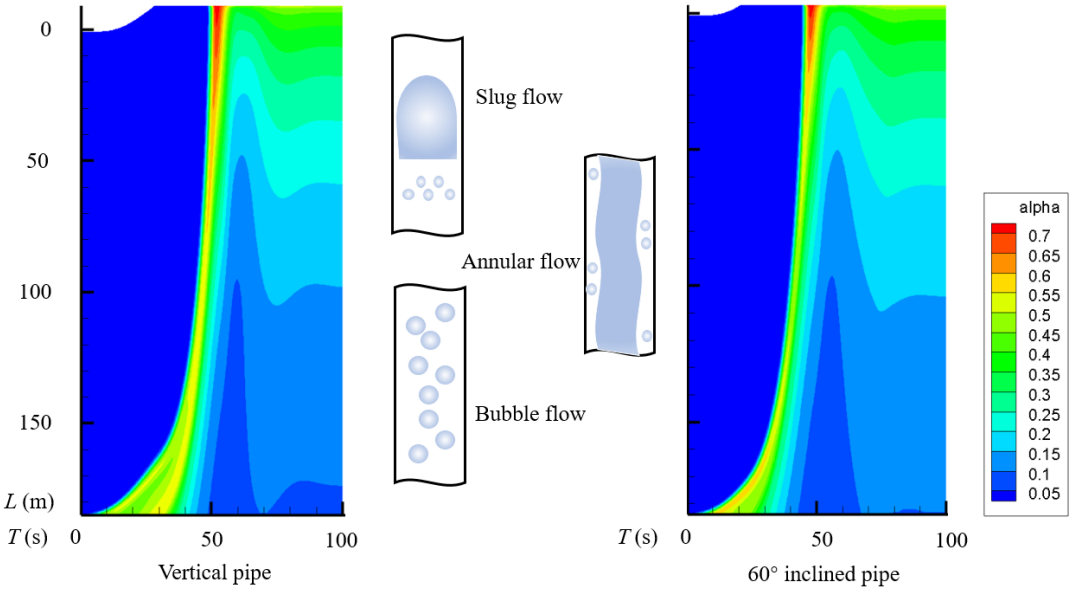


Figure 5. Axial and temporal gas holdup evolution for the vertical and 60° inclined cases. The central bubble, slug, and annular sketches are generic illustrations only; they are not assigned to either contour panel nor used to classify its flow regime.

Table 3. Inclination comparison conditions and vertical injection depths calculated from hinj = ZL sin θ.

Case	D (m)	L (m)	ZL (m)	$\dot{m}_g$ (kg/s)	θ (°)	hinj (m)
1-1	0.1023	197	185	0.3	90	185.00
1-2					80	182.19
1-3					70	173.84
1-4					60	160.21

Figure 5 shows the propagation of a gas-rich region, subsequent redistribution, and approach to a more stable axial profile. The major initial change occurs over approximately 0–50 s, followed by redistribution over approximately 50–75 s. Both panels are interpreted consistently as gas holdup evolution. The central sketches illustrate familiar

flow morphologies but provide no classification of either simulation. In particular, the color scale ending at $\alpha g = 0.70$ does not establish an annular-flow state. Closure-branch selection and observed morphology must remain distinct.

Figure 6 compares gas fraction, frictional pressure gradient, and phase velocities. Changes between the vertical and 80° cases are smaller than those between the vertical and 60° cases. At fixed ZL = 185 m, the vertical injection depths are 185.00, 182.19, 173.84, and 160.21 m. The 60° case therefore has a 13.40% smaller injection depth than the vertical case. This is a geometric head change, not a measured reduction in liquid throughput. The corresponding slip multipliers $f\theta$ are 1.000, 1.203, 1.380, and 1.514. These two effects explain why changing inclination cannot be interpreted solely as a local drift correction: the hydrostatic driving and relative phase motion change together. The original dimensionally unspecified capacity values have been removed; liquid delivery is defined in Section 5.4.

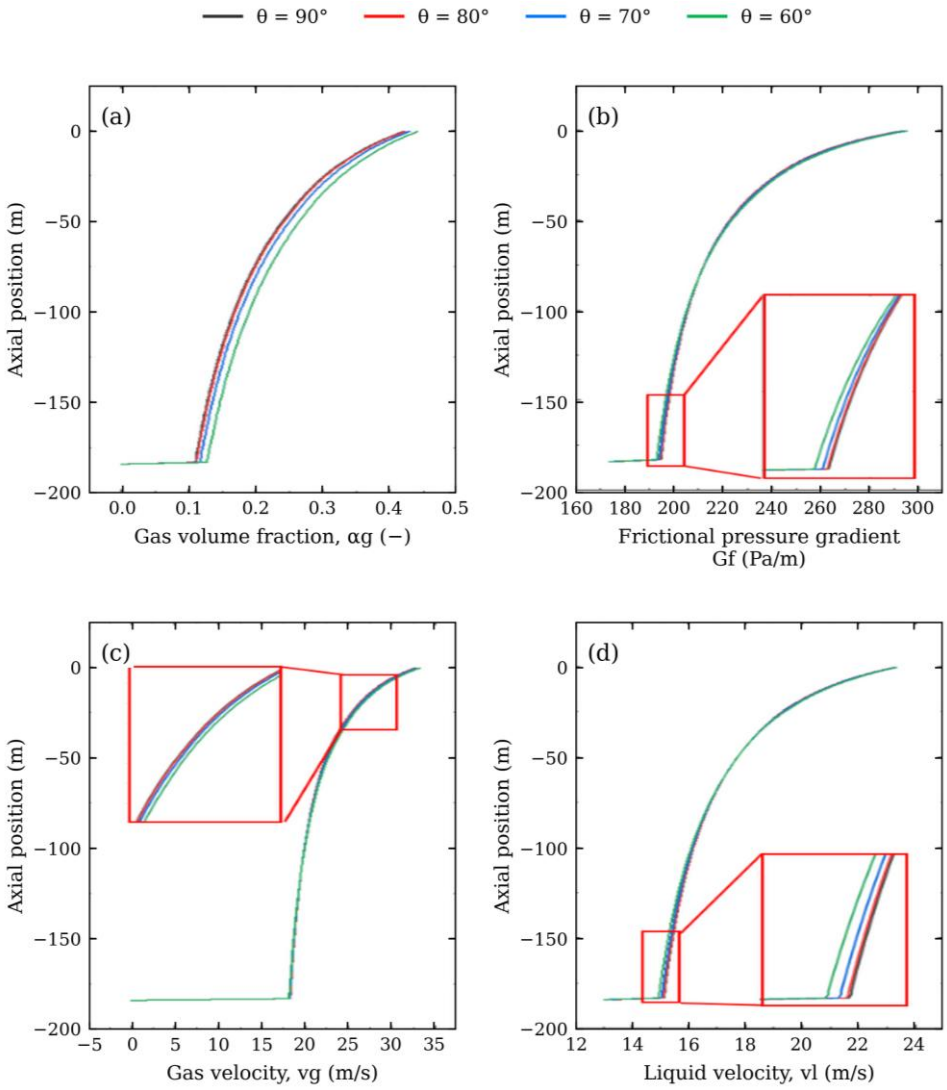


Figure 6. Axial profiles for θ = 90°, 80°, 70°, and 60°: (**a**) gas volume fraction, (**b**) frictional pressure gradient Gf, (**c**) gas velocity, and (**d**) liquid velocity; D = 0.1023 m, L = 197 m, ZL = 185 m, and $\dot{m}_{g,inj}$ = 0.3 kg s^{-1}. The shared legend identifies inclination, and the insets enlarge the indicated profile regions.

5.2. Effect of Gas Injection Mass Flow Rate

The injection rate comparison uses gas mass flow rates of 0.1, 0.2, 0.3, and 0.4 kg s^{-1}. This quantity is distinct from a volumetric flow rate, which depends on the pressure and temperature at the reference location. Figures 7 and 8 show the gas holdup response for vertical and inclined configurations. Increased injection changes both the gas-rich region and the start-up response. Figure 9 provides the corresponding phase-velocity and frictional-pressure-gradient profiles. The comparisons identify 0.3 kg s^{-1} as a candidate setting in the tested series, but no compressor-work calculation or cost function is supplied. Accordingly, the results support a hydrodynamic comparison and do not establish a thermodynamic or economic optimum.

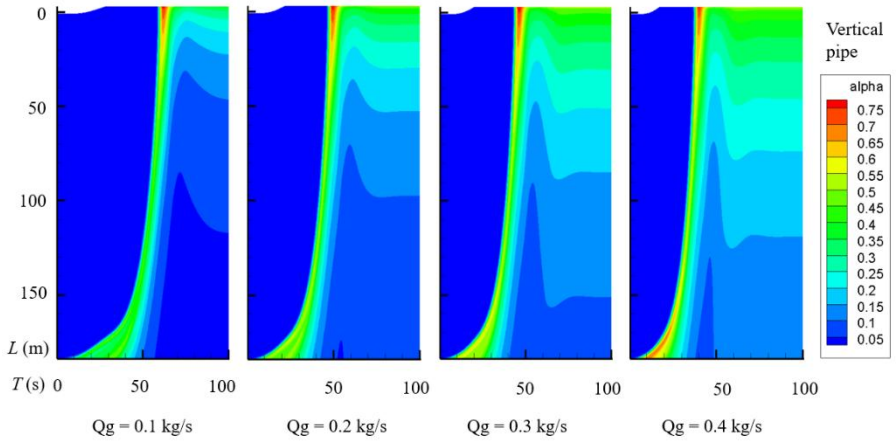


Figure 7. Axial and temporal gas-volume-fraction contours for the vertical pipe at gas injection rates of 0.1, 0.2, 0.3, and 0.4 kg s^{-1}; D = 0.1023 m, L = 197 m, and ZL = 185 m. The color scale represents cross-section-averaged gas fraction.

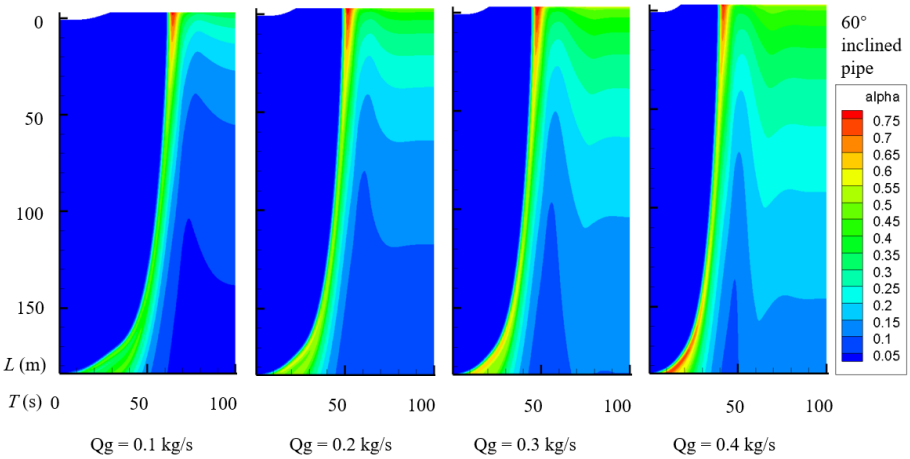


Figure 8. Axial and temporal gas-volume-fraction contours for the 60° inclined pipe at gas injection rates of 0.1, 0.2, 0.3, and 0.4 kg s^{-1}, with the same diameter, axial length, and injection distance as Figure 7.

The inlet-region transient becomes more pronounced in the inclined case at the higher tested injection rate. This observation motivates examination of start-up behavior alongside the later liquid delivery rate. It does not define a safe operating boundary because allowable pressure, velocity, and structural loads are not specified. Figure 9 shows that inclination and gas injection modify gas holdup, liquid velocity, and frictional pressure gradient together. These variables should therefore be considered jointly when comparing operating conditions.

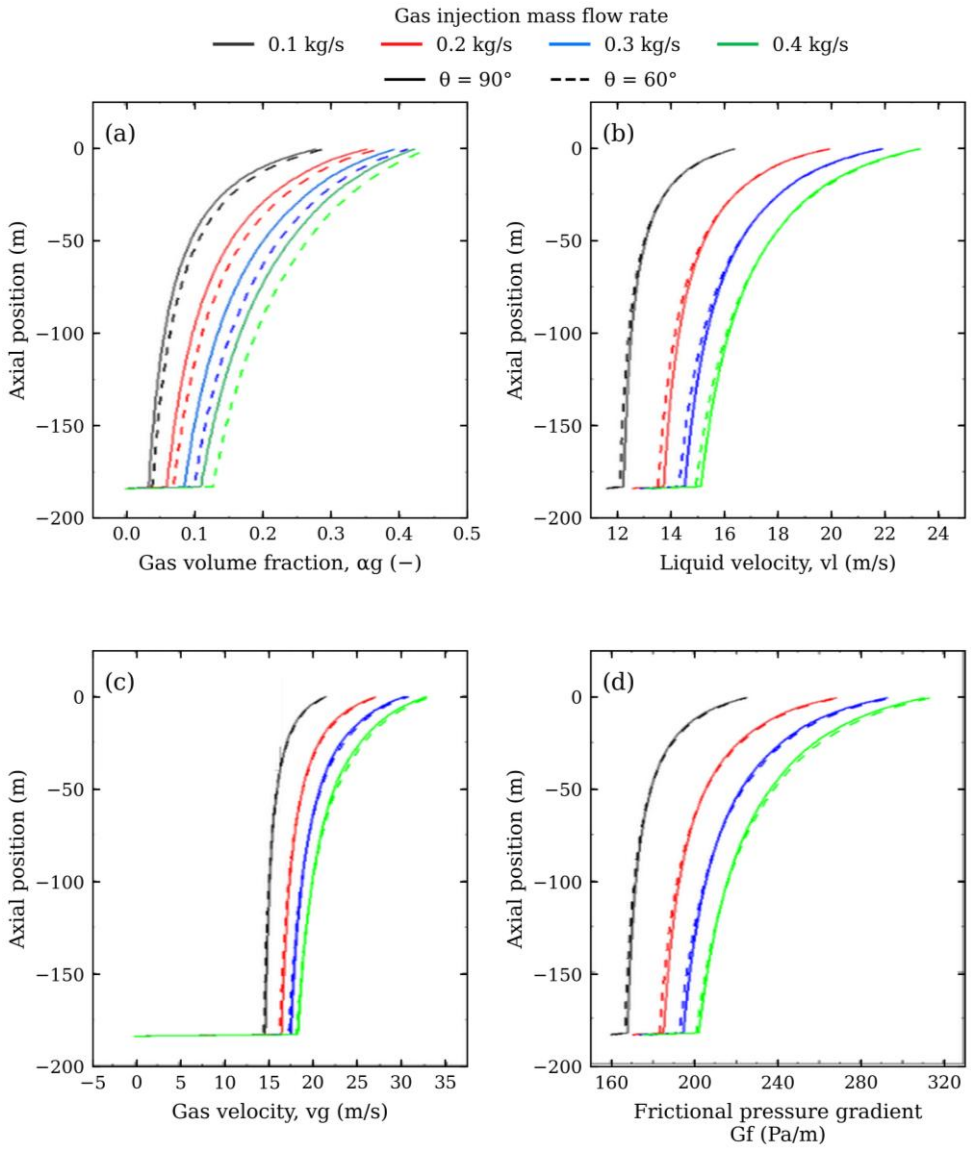


Figure 9. Axial profiles for gas injection rates of 0.1–0.4 kg s^{-1}: (**a**) gas volume fraction, (**b**) liquid velocity, (**c**) gas velocity, and (**d**) frictional pressure gradient Gf. Colors identify injection rate; solid and dashed curves denote θ = 90° and 60°, respectively. D = 0.1023 m, L = 197 m, and ZL = 185 m.

5.3. Effect of Gas Injection Location

Figures 10–13 compare axial injection distances ZL = 160, 165, 170, 175, 180, and 185 m at $\dot{m}_{g,inj}$ = 0.3 kg s^{-1}. Their vertical depths are hinj = ZL sin θ; at 60°, the series spans 138.56–160.21 m, and ZL = 170 m corresponds to 147.22 m. Changing ZL alters both the length of the gas-containing segment and the gas entry pressure. The contours describe the resulting start-up and gas holdup response; they do not independently identify a flow pattern transition. The 170 m case is one examined setting rather than a demonstrated global optimum.

A deeper injector exposes the entering gas to a higher local pressure and lengthens the gas-containing lifting segment. At a fixed injected mass rate and temperature, the entering gas volume rate decreases as local gas density increases. Neither this relation nor proximity to the suction port guarantees bubbly flow: initial bubble size, coalescence, pipe diameter, phase velocities, and subsequent expansion also matter. No bubble size population or injector-scale flow is solved here. Injection position comparisons are therefore interpreted through pressure head, slip, and friction, without assigning a favorable flow regime solely from injector location.

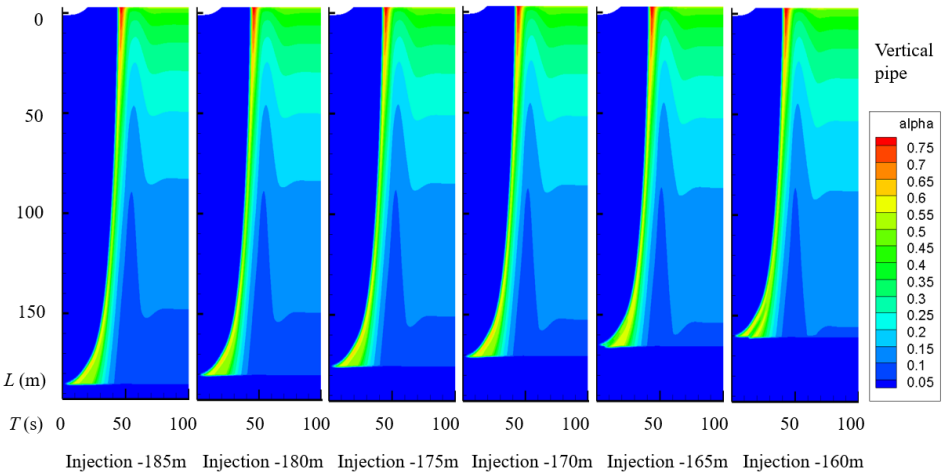


Figure 10. Axial and temporal gas volume fraction contours for the vertical pipe at ZL = 160, 165, 170, 175, 180, and 185 m; D = 0.1023 m, L = 197 m, and $\dot{m}_{g,inj}$ = 0.3 kg s^{-1}. ZL is measured along the pipe below the still-water intersection.

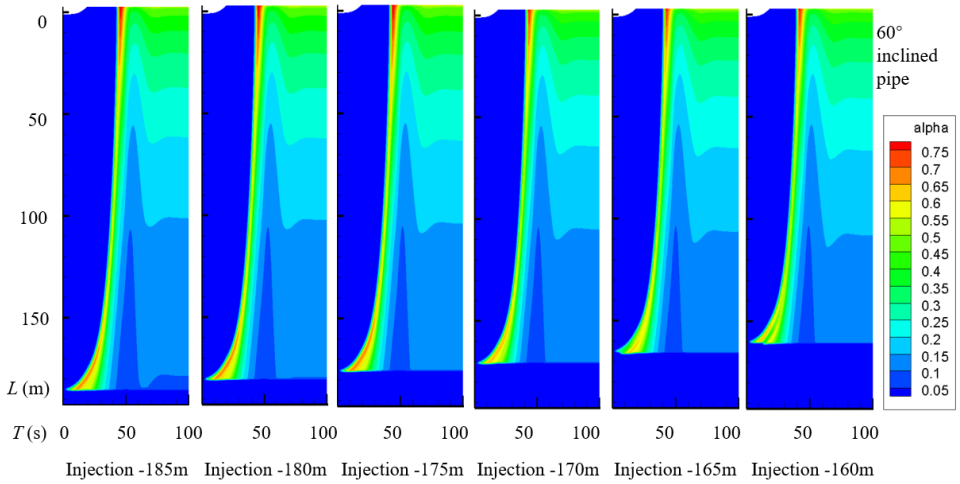


Figure 11. Axial and temporal gas volume fraction contours for the 60° inclined pipe at the six axial injection distances in Figure 10; the corresponding vertical injection depth is hinj = ZL sin 60°.

Figures 12 and 13 show that the injection location changes have their largest influence near the gas-entry region, while some upper-pipe profiles remain close together. Steady mass conservation fixes each phase mass flux away from the source; it does not require the same liquid throughput or outlet velocity in different injection location cases. The liquid flow rate also depends on the pressure and friction balance. The observed similarity of selected outlet profiles is therefore a result of these particular cases, not a general consequence of equal gas injection. Inclination changes the same balance and should be considered when selecting an injection position.

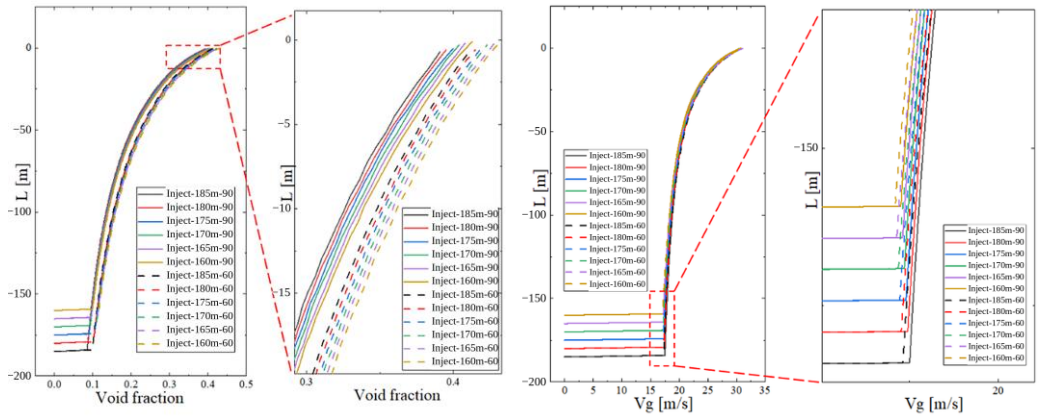


Figure 12. Axial gas volume fraction (**left**) and gas velocity (**right**) profiles for the injection location series ZL = 160–185 m at $\dot{m}_{g,inj}$ = 0.3 kg s^{-1}; D = 0.1023 m and L = 197 m. Each curve is identified in the legend as "Inject-Z_Lm-θ", where the hyphens separate the injection distance Z_L (m) and the inclination θ (°); the right-hand panels enlarge the boxed regions.

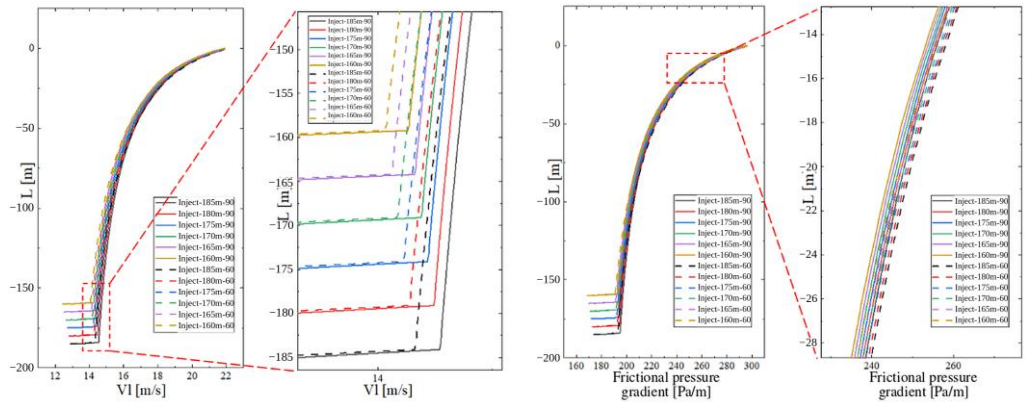


Figure 13. Axial liquid velocity (**left**) and frictional pressure gradient Gf (**right**) profiles for the same injection location series and fixed parameters as in Figure 12. Gf is plotted in Pa/m and is not wall shear stress.

5.4. Liquid Throughput Definitions and Interpretation

The preceding parameter comparisons describe hydrodynamic responses at selected operating points. They do not constitute a constrained optimization because no objective weighting, compressor-power model, economic criterion, or quantified safety constraint is evaluated. Accordingly, no global or energy optimum is claimed. The injection rate and axial injection distance must be reported together with inclination because the latter sets the corresponding vertical head.

The outlet liquid volumetric throughput is $Q_{l,out} = A(1 - \alpha_{g,out})v_{l,out}$ in $m^3\ s^{-1}$, and the mass throughput is $\dot{m}_{l,out} = \varrho_{l,out}Q_{l,out}$ in kg s^{-1}. These definitions match the liquid discharge postprocessor. A time-averaged result would additionally require an explicit averaging interval. The ratio $\dot{m}_{l,out}/\dot{m}_{g,inj}$ is dimensionless gas supply-normalized throughput. It is not an energy efficiency, which would require useful hydraulic power and compressor input power. The dimensionally unspecified capacity column and the unsupported diameter–length candidate matrix have been removed.

5.5. Engineering Scope and Extension Requirements

The straight, fixed-inclination model provides a reference for carrier-flow screening, not a time-varying shape model for an offshore riser. In a curved pipe, the local axial

gravity projection depends on the tangent angle along the arc length; curvature also introduces secondary flow and additional losses. Pipe motion adds acceleration and pressure feedback and changes the internal and external loads. A defensible extension would couple the one-dimensional balances to a beam or cable model, update local orientation and boundary elevations, and include independently supported curvature and motion terms. The static-angle comparisons isolate one geometric influence, but do not replace fluid–structure interaction or predict fatigue and dynamic stability.

Polydisperse solids introduce size-dependent slip, increased mixture weight, particle–fluid and particle–wall momentum exchange, and possible settling or accumulation. Agglomeration can change effective particle size, while concentration and shear history can change slurry rheology. These processes can alter both the pressure requirement and the minimum velocity needed to avoid deposition; their net effect cannot be assigned a universal correction factor or bias from the present gas–liquid results. The calculated liquid throughput is therefore not a solids production rate, and the phase velocities are not validated particle transport thresholds. For engineering use, the present comparisons can identify carrier-flow trends for subsequent testing, whereas a recovery design requires solids balances, a particle size distribution, measured rheology, and validation under the intended pressure and inclination.

6. Conclusions

A one-dimensional gas–liquid drift-flux framework has been used to examine static pipeline inclination and gas injection choices. The main findings, within the stated carrier-fluid assumptions, are as follows:

The application cases cover θ = 60–90°, measured from the horizontal. Inclination affects the axial gravity projection and the adopted relative-motion closure. Waves, currents, and structural motion are not solved dynamically.

For the 197 m pipe with D = 0.1023 m and $\dot{m}_{g,inj}$ = 0.3 kg s^{-1}, the inclination comparison holds the axial injection distance ZL = 185 m fixed. Consequently, the vertical injection depth falls from 185.00 to 160.21 m between 90° and 60°, while the adopted inclination multiplier rises from 1.000 to 1.514. These are geometric and closure changes; no percentage reduction in liquid throughput is inferred from them.

The injection rate comparison covers 0.1–0.4 kg s^{-1}. The gas holdup and phase-velocity results show that increased injection changes the start-up transient as well as the later axial profile. The 0.3 kg s^{-1} case is a candidate operating point within this comparison, rather than an independently established energy optimum.

The injection position series covers axial distances of 160–185 m. At 60°, these correspond to vertical depths of 138.56–160.21 m. The largest profile differences appear near gas entry. The examined settings support case comparisons rather than a validated optimization map.

The experimental comparisons concern inclined bubble drift and vertical airlift throughput. The nonmonotonic time step comparison does not establish temporal independence. Void-fraction contours indicate gas holdup evolution and cannot independently validate bubbly, slug, or annular morphology.

The model excludes an explicit solid phase, concentration-dependent rheology, dissolution, thermal variation, and fluid–structure interaction. The constant-property Newtonian carrier and ideal-gas approximation limit extrapolation to deep, high-pressure slurry transport. Empirical friction and drift closures do not resolve radial segregation or local injector flow.

Further assessment requires consistent numerical convergence evidence and further measurements at the relevant inclination, pressure, diameter, and carrier-fluid properties. Explicit particle transport and independently characterized slurry rheology are required

for a solids recovery calculation. Compressor power is additionally required for an energy efficiency assessment.

Funding: This research was supported by the Japan Science and Technology Agency (grant number JPMJSP2108).

Data Availability Statement: The data presented in this study are available upon request from the corresponding author.

Acknowledgments: The author gratefully acknowledges the support of the WINGS-QSTEP (Quantum Science and Technology Fellowship Program) at the University of Tokyo.

Conflicts of Interest: The author declares no conflicts of interest.

Nomenclature

Nomenclature for the governing equations and closure relations in Sections 2 and 3; the units below distinguish dimensional quantities from nondimensional coefficients.

ρ	Density	[kg/m³]
α	Volume fraction	[-]
v	Velocity	[m/s]
C_0	Gas phase distribution constant	[-]
C_1	Experience coefficient 1	[-]
C_2	Experience coefficient 2	[-]
τ_w	Pipe friction resistance (stress)	[Pa]
V_{Gj}	Bulk drift difference, vg − Jm	[m/s]
J_k	Superficial velocity of k phase	[m/s]
σ	Surface tension	[N/m]
λ_k	Wall friction factor of pipe	[-]
ε	Absolute inner-wall roughness	[m]
Re_k	Reynolds number of k phase	[-]
N_D	Dimensionless pipe diameter	[-]
Frgj	Reference drift Froude number	[-]
θ	Inclination angle	[°]
l_c	Capillary length	[m]
vgj	Closure drift term; 90 or θ denotes orientation	[m/s]
s	Pipe-axis coordinate, positive upward	[m]
L	Total pipe length	[m]
A	Pipe cross-sectional area	[m²]
Γg, Γm	External volumetric mass source	[kg/(m³ s)]
T	Prescribed absolute temperature	[K]
Ra	Specific gas constant of air	[J/(kg K)]
Uσ	Capillary–buoyancy velocity scale	[m/s]
μ*	Dimensionless liquid viscosity	[−]
Cf	Two-phase friction multiplier coefficient	[−]
Gf	Frictional pressure gradient, 4τw/D	[Pa/m]
ZL	Axial injection distance below still water	[m]
ZH	Axial submerged pipe length	[m]
hinj	Vertical injection depth, ZL sin θ	[m]
CA	Auxiliary coefficient in the high-void-fraction closure	[−]
Γl, ΓL	Liquid external mass source, zero here	[kg/(m³ s)]
i, N	Spatial index and terminal spatial index	[−]
n, n + 1	Known and updated time levels (superscripts)	[−]

Δs, Δz; Δt	Axial spacing; time step	[m]; [s]
ϕ; β	Interpolated variable; signed direction selector	Variable; [−]
Aw, Ap, Ae, Aee	Interpolation stencil weights	[−]
Si	Lagged interpolation correction	As ϕ
Smce, Sgce	Collected mixture and gas balance terms	As equation
ϑ	Time weight; distinct from inclination θ	[−]
AS, AP, AN	Tridiagonal momentum coefficients	As equation

Appendix A

The expressions below document the original vertical reference discretization. The parameter ϑ is the time-discretization weight, not the inclination angle θ; ϑ = 1 gives the implicit time update. With an upward coordinate, the base momentum routine contributes −ϱmgΔs. The corresponding inclined gravity contribution is −ϱmg sin θ Δs, consistent with Equation (10). Hydrostatic boundary pressures must use the corresponding vertical elevations.

In the expressions below, N denotes the terminal spatial index and n denotes time only when written as a superscript. The symbols Δz and Δs both denote axial cell length in the original and main-text notation, respectively. AS, AP, and AN are the coefficients of the lower-index neighbor, current point, and higher-index neighbor in the tridiagonal momentum equation. Smom, SmomF, and SmomB collect its right-hand-side contributions; the subscripts in and out identify inlet and outlet boundary forms. The pressure gradient, gravity, and friction terms must retain the common upward-axis sign convention stated in Section 2.1.

$$\frac{(\rho_m v_m)_0^{n+1} - (\rho_m v_m)_0^n}{\Delta t} + \frac{(\rho_m v_m^2)_1^{n+1} - (\rho_m v_m^2)_0^{n+1}}{\Delta z} = -\frac{(P)_0^{n+1} - (P)_{in}^{n+1}}{\Delta z/2} - (\rho_m)_0^{n+1} g - \left(\frac{4\tau_w}{D}\right)_0^{n+1} - \frac{1}{\Delta z}\left[\left(\frac{\alpha_g \rho_g \rho_l}{\alpha_l \rho_m} V_G^2\right)_1^{n+1} - \left(\frac{\alpha_g \rho_g \rho_l}{\alpha_l \rho_m} V_G^2\right)_0^{n+1}\right]$$

$$\frac{(\rho_m v_m)_0^{n+1} - (\rho_m v_m)_0^n}{\Delta t} + \frac{(\rho_m v_m^2)_0^{n+1} - (\rho_m v_m^2)_{-1}^{n+1}}{\Delta z} = -\frac{(P)_0^{n+1} - (P)_{in}^{n+1}}{\Delta z/2} - (\rho_m)_0^{n+1} g - \left(\frac{4\tau_w}{D}\right)_0^{n+1} - \frac{1}{\Delta z}\left[\left(\frac{\alpha_g \rho_g \rho_l}{\alpha_l \rho_m} V_G^2\right)_0^{n+1} - \left(\frac{\alpha_g \rho_g \rho_l}{\alpha_l \rho_m} V_G^2\right)_{-1}^{n+1}\right]$$

$$\frac{(\rho_m v_m)_N^{n+1} - (\rho_m v_m)_N^n}{\Delta t} + \frac{(\rho_m v_m^2)_N^{n+1} - (\rho_m v_m^2)_{N-1}^{n+1}}{\Delta z} = -\frac{(P)_{out}^{n+1} - (P)_{N-1}^{n+1}}{\Delta z/2} - (\rho_m)_{N-1}^{n+1} g - \left(\frac{4\tau_w}{D}\right)_{N-1}^{n+1} - \frac{1}{\Delta z}\left[\left(\frac{\alpha_g \rho_g \rho_l}{\alpha_l \rho_m} V_G^2\right)_N^{n+1} - \left(\frac{\alpha_g \rho_g \rho_l}{\alpha_l \rho_m} V_G^2\right)_{N-1}^{n+1}\right]$$

$$\begin{aligned}
&\frac{\Delta z}{\Delta t}(\rho_m v_m)_0^{n+1} + \vartheta[(\rho_m v_m^2)_1^{n+1} - (\rho_m v_m^2)_0^{n+1}] \\
&= -2\vartheta\left[(P)_0^{n+1} - (P)_{in}^{n+1}\right] \\
&-\vartheta\left\{(\rho_m)_0^{n+1} g\Delta z + \Delta z\left(\frac{4\tau_w}{D}\right)_0^{n+1} + \left[\left(\frac{\alpha_g \rho_g \rho_l}{\alpha_l \rho_m} V_G^2\right)_1^{n+1} - \left(\frac{\alpha_g \rho_g \rho_l}{\alpha_l \rho_m} V_G^2\right)_0^{n+1}\right]\right\} \\
&+(1-\vartheta)\left\{-[(\rho_m v_m^2)_1^{n+1} - (\rho_m v_m^2)_0^{n+1}] - 2[(P)_0^n - (P)_{in}^n] - (\rho_m)_0^n g\Delta z - \Delta z\left(\frac{4\tau_w}{D}\right)_0^n - \left[\left(\frac{\alpha_g \rho_g \rho_l}{\alpha_l \rho_m} V_G^2\right)_1^n - \left(\frac{\alpha_g \rho_g \rho_l}{\alpha_l \rho_m} V_G^2\right)_0^n\right]\right\} \\
&+\frac{\Delta z}{\Delta t}(\rho_m v_m)_0^n
\end{aligned}$$

$$\frac{\Delta z}{\Delta t}(\rho_m v_m)_N^{n+1} + \vartheta[(\rho_m v_m^2)_N^{n+1} - (\rho_m v_m^2)_{N-1}^{n+1}]$$
$$= -2\vartheta[(P)_{out}^{n+1} - (P)_{N-1}^{n+1}]$$
$$-\vartheta\left\{(\rho_m)_N^{n+1} g\Delta z + \Delta z\left(\frac{4\tau_w}{D}\right)_N^{n+1} + \left[\left(\frac{\alpha_g\rho_g\rho_l}{\alpha_l\rho_m}V_G^2\right)_N^{n+1} - \left(\frac{\alpha_g\rho_g\rho_l}{\alpha_l\rho_m}V_G^2\right)_{N-1}^{n+1}\right]\right\}$$
$$+(1-\vartheta)\left\{-[(\rho_m v_m^2)_N^{n+1} - (\rho_m v_m^2)_{N-1}^{n+1}] - 2[(P)_{out}^{n} - (P)_{N-1}^{n}] - (\rho_m)_N^n g\Delta z - \Delta z\left(\frac{4\tau_w}{D}\right)_N^n - \left[\left(\frac{\alpha_g\rho_g\rho_l}{\alpha_l\rho_m}V_G^2\right)_N^n - \left(\frac{\alpha_g\rho_g\rho_l}{\alpha_l\rho_m}V_G^2\right)_{N-1}^n\right]\right\}$$
$$+\frac{\Delta z}{\Delta t}(\rho_m v_m)_N^n$$

The reported momentum discretization is written as follows:

$$(A_S)_{i-1/2}^{n+1}(v_m)_{i-1/2}^{n+1} + (A_P)_{i+1/2}^{n+1}(v_m)_{i+1/2}^{n+1} + (A_N)_{i+3/2}^{n+1}(v_m)_{i+3/2}^{n+1} = -\vartheta((P)_{i+1}^{n+1} - (P)_i^{n+1}) + (S_{mom})_i$$

$$(A_S)_{i-1/2}^{n+1} = -\vartheta(\rho_m)_i^{n+1}(v_m)_i^{n+1}\max[\beta_i, 0]$$

$$(A_N)_{i+3/2}^{n+1} = \vartheta(\rho_m)_{i+1}^{n+1}(v_m)_{i+1}^{n+1}\max[-\beta_{i+1}, 0]$$

$$(A_P)_{i+1/2}^{n+1} = \frac{\Delta z}{\Delta t}(\rho_m)_{i+1/2}^{n+1} + \vartheta(\rho_m)_{i+1}^{n+1}(v_m)_{i+1}^{n+1}\max[\beta_{i+1}, 0] - \vartheta(\rho_m)_i^{n+1}(v_m)_i^{n+1}\max[-\beta_i, 0]$$

$$(S_{mom})_i = \left(S_{mom}^{def}\right)_i^n + (S_{mom}^F)_{i+1/2}^{n+1} + (S_{mom}^B)_{i+1/2}^n$$

$$\left(S_{mom}^{def}\right)_i^n = -\vartheta\left[(\rho_m)_{i+1}^{n+1}(v_m)_{i+1}^{n+1}\left(v_m^{def}\right)_{i+1}^n - (\rho_m)_i^{n+1}(v_m)_i^{n+1}\left(v_m^{def}\right)_i^n\right]$$

$$(S_{mom}^F)_{i+1/2}^{n+1} = -\vartheta\left[\left(\frac{\rho_g\rho_l}{\rho_m}\frac{\alpha V_G^2}{1-\alpha}\right)_{i+1}^{n+1} - \left(\frac{\rho_g\rho_l}{\rho_m}\frac{\alpha V_G^2}{1-\alpha}\right)_i^{n+1}\right] - g\vartheta\Delta z(\rho_m)_{i+1/2}^{n+1} - \vartheta\Delta z(4\tau_w/D)_{i+1/2}^{n+1}$$

$$(S_{mom}^B)_{i+1/2}^n = -(1-\vartheta)\left[\left(\frac{\rho_g\rho_l}{\rho_m}\frac{\alpha V_G^2}{1-\alpha}\right)_{i+1}^n - \left(\frac{\rho_g\rho_l}{\rho_m}\frac{\alpha V_G^2}{1-\alpha}\right)_i^n\right]$$
$$-g(1-\vartheta)\Delta z(\rho_m)_{i+1/2}^n - (1-\vartheta)\Delta z(4\tau_w/D)_{i+1/2}^n$$
$$-(1-\vartheta)[(\rho_m v_m^2)_{i+1}^n - (\rho_m v_m^2)_i^n] - (1-\vartheta)((P)_{i+1}^n - (P)_i^n)$$
$$+\frac{\Delta z}{\Delta t}(\rho_m v_m)_{i+1/2}^n$$

References

1. Ambrosini, W.; Forasassi, G.; Forgione, N.; Oriolo, F.; Tarantino, M. Experimental study on combined natural and gas-injection enhanced circulation. *Nucl. Eng. Des.* **2005**, *235*, 1179–1188.
2. Benamati, G.; Foletti, C.; Forgione, N.; Oriolo, F.; Scaddozzo, G.; Tarantino, M. Experimental study on gas-injection enhanced circulation performed with the CIRCE facility. *Nucl. Eng. Des.* **2007**, *237*, 768–777.
3. Shimizu, Y.; Hatakeyama, N.; Masuyama, T. Numerical Analysis on Air-Lift Pumping System for Mining Rare-Earth Rich Mud. *J. MMIJ* **2018**, *134*, 142–215.
4. Hanafizadeh, P.; Raffiee, A.H.; Saidi, M.H. Experimental investigation of characteristic curve for gas-lift pump. *J. Pet. Sci. Eng.* **2014**, *116*, 19–27.
5. Gao, H.; Liu, B.; Yan, Y. Numerical simulation of bubbles motion in lifting pipe of bubble pump for lithium bromide absorption chillers. *Appl. Therm. Eng.* **2017**, *115*, 1398–1406.
6. Hanafizadeh, E.A. Effect of bubble size and angle of tapered upriser pipe on the effectiveness of a two phase lifting pump. In Proceedings of the ASME 2009 Fluids Engineering Division Summer Meeting, Vail, CO, USA, 2–6 August 2009.
7. Chen, W.; Xu, H.-L.; Kong, W.-Y.; Yang, F.-Q. Study on three-phase flow characteristics of natural gas hydrate pipeline transmission. *Ocean Eng.* **2020**, *214*, 107727.

8. Zhou, D.; Ma, Y.; Li, S.; You, Y.; Chen, W.; Feng, A. Vibration stability of a lifting pipe transporting solid–liquid two phase flow. *Ocean Eng.* **2023**, *288*, 116170.
9. Jørgen, T.M.; Challabotla, N.R.; Sævik, S.; Nydal, O.J. A numerical study on vortex-induced vibrations and the effect of slurry density variations on fatigue of ocean mining risers. *Ocean Eng.* **2019**, *174*, 1–13.
10. Enany, P.; Shevchenko, O.; Drebenstedt, C. Experimental Evaluation of Airlift Performance for Vertical Pumping of Water in Underground Mines. *Mine Water Environ.* **2021**, *40*, 970–979. https://doi.org/10.1007/s10230-021-00807-w.
11. Kajishima, T.; Saito, T. Numerical Simulation of Unsteady Flow in Air-Lift Pump. *JSME Int. J. Ser. B Fluids Therm. Eng.* **1996**, *39*, 525–532. https://doi.org/10.1299/jsmeb.39.525.
12. Saito, T.; Kajishima, T.; Tsuchiya, K. Pumping characteristics of a large-scale gas-lift system. *Exp. Therm. Fluid Sci.* **2004**, *28*, 479–488.
13. Chizuna, K.; Ito, K. Cold model experiments on the application of gas lift pump to the transportation of molten metal. *ISIJ Int.* **1995**, *35*, 859–865.
14. Moisidis, C.T.; Kastrinakis, E.G. Two-phase flow pattern transitions of short airlift pumps. *J. Hydraul. Res.* **2010**, *48*, 680–685.
15. Moisidis, C.T.; Kastrinakis, E.G. Pressure behaviour in riser tube of a short airlift pump. *J. Hydraul. Res.* **2010**, *48*, 65–73.
16. Wahba, E.M.; Gadalla, M.A.; Abueidda, D.; Dalaq, A.; Hafiz, H.; Elawadi, K.; Issa, R. On the performance of air-lift pumps: From analytical models to large eddy simulation. *J. Fluids Eng.* **2014**, *136*, 111301.
17. Zhang, B.; Fu, Y.; Zhang, M.H.; Liu, J.Y. Numerical investigations into the influence of geometric configurations on hydrodynamic characteristics of torpedo anchors. *Mar. Struct.* **2023**, *90*, 103445.
18. Bendiksen, K.H. An experimental investigation of the motion of long bubbles in inclined tubes. *Int. J. Multiph. Flow* **1984**, *10*, 467–483.
19. Bhagwat, S.M.; Ghajar, A.J. Similarities and differences in the flow patterns and void fraction in vertical upward and downward two phase flow. *Exp. Therm. Fluid Sci.* **2012**, *39*, 213–227.
20. Bhagwat, S.M.; Ghajar, A.J. A flow pattern independent drift flux model based void fraction correlation for a wide range of gas–liquid two phase flow. *Int. J. Multiph. Flow* **2014**, *59*, 186–205.
21. Fujimoto, H.; Murakami, S.; Omura, A.; Takuda, H. Effect of local pipe bends on pump performance of a small air-lift system in transporting solid particles. *Int. J. Heat Fluid Flow* **2004**, *25*, 996–1005. https://doi.org/10.1016/j.ijheatfluidflow.2004.02.025.
22. Kassab, S.Z.; Abdelrazek, A.A.; Lotfy, E.R. Performance and Hydrodynamics of a Bent Riser Airlift Pump. *J. Appl. Fluid Mech.* **2025**, *18*, 2453–2464. https://doi.org/10.47176/jafm.18.10.3384.
23. Shimizu, Y.; Sugihara, M.; Fujinaga, K.; Nakamura, K.; Kato, Y. Air-Lift Pumping System for Hybrid Mining of Rare-Earth Elements-Rich Mud and Polymetallic Nodules around Minamitorishima Island. *J. Mar. Sci. Eng.* **2024**, *12*, 1470. https://doi.org/10.3390/jmse12091470.
24. Shimizu, Y.; Sugihara, M.; Fujinaga, K.; Nakamura, K.; Kato, Y. Numerical Simulation on Hybrid Lifting Operation of Polymetallic Nodules and Rare-Earth Elements-Rich Mud by Air-Lift Pump in Deep Sea around Minamitorishima Island. *J. Mar. Sci. Eng.* **2025**, *13*, 267. https://doi.org/10.3390/jmse13020267.
25. Hibiki, T.; Dong, C.; Tsukamoto, N. Full-Range Drift–Flux Correlation for Upward Cocurrent Two-Phase Flows in Vertical Pipes. *Int. J. Energy Res.* **2025**, *2025*, 6193526. https://doi.org/10.1155/er/6193526.
26. Heydari, O.; Zendehboudi, S.; Butt, S. A Unified Drift–Flux Framework for Predictive Analysis of Flow Patterns and Void Fractions in Vertical Gas Lift Systems. *Fluids* **2026**, *11*, 6. https://doi.org/10.3390/fluids11010006.
27. Takano, S.; Masanobu, S.; Kanada, S.; Ono, M. Correlation for calculating frictional pressure drops in vertical three-phase flows for subsea-resource production. *Ocean Eng.* **2023**, *275*, 114121.
28. Benjamin, T.B. Gravity currents and related phenomena. *J. Fluid Mech.* **1968**, *31*, 209–248.
29. Hibiki, T.; Takamasa, T.; Ishii, M. One-dimensional drift-flux model and constitutive equations for relative motion between phases in various two-phase flow regimes at microgravity conditions. In Proceedings of the International Conference on Nuclear Engineering, Arlington, VA, USA, 25–29 April 2004; Volume 4689, pp. 377–386.
30. Kaji, R.; Azzopardi, B.J. The effect of pipe diameter on the structure of gas/liquid flow in vertical pipes. *Int. J. Multiph. Flow* **2010**, *36*, 303–313.
31. Hatakeyama, N.; Shimizu, Y.; Masuyama, T. Constitutive Equations for a Simulator of Airlift Pump in a Large Diameter Pipe using Drift-Flux Model. *J. MMIJ* **2018**, *134*, 31–40. https://doi.org/10.2473/journalofmmij.134.31.
32. Isao, K.; Mamoru, I. Drift flux model for large diameter pipe and new correlation for pool void fraction. *Int. J. Heat Mass Transf.* **1987**, *30*, 1927–1939.

33. Hibiki, T.; Ishii, M. Distribution parameter and drift velocity of drift-flux model in bubbly flow. *Int. J. Heat Mass Transf.* **2002**, *45*, 707–721.
34. Hibiki, T.; Ishii, M. One-dimensional drift–flux model for two-phase flow in a large diameter pipe. *Int. J. Heat Mass Transf.* **2003**, *46*, 1773–1790.
35. Alves, I.N.; Shoham, O.; Taitel, Y. Drift velocity of elongated bubbles in inclined pipes. *Chem. Eng. Sci.* **1993**, *48*, 3063–3070.
36. Sanderse, B.; Eskerud Smith, I.; Hendrix, M.H.W. Analysis of time integration methods for the compressible two-fluid model for pipe flow simulations. *Int. J. Multiph. Flow* **2017**, *95*, 155–174. https://doi.org/10.1016/j.ijmultiphaseflow.2017.05.002.
37. Weber, M.; Dedegil, Y. Transport of solids according to the air-lift principle. In Proceedings of the 4th International Conference on the Hydraulic Transport of Solids in Pipes, Banff, AB, Canada, 18–21 May 1976; pp. 1–23.
38. Usami, T.; Saito, T.; Kitahara, R. Lifting characteristics of solid by air lift pump (2rd report). *J. Min. Metall. Inst. Jpn.* **1982**, *98*, 29–34.
39. Saito, T.; Usami, T.; Yamazaki, T.; Tomishima, Y.; Kiyono, F.; Shimizu, Y. Analysis of lifting characteristics of manganese nodules by air lift pump by means of dimensionless parameter. *J. Min. Metall. Inst. Jpn.* **1991**, *107*, 265–270.

Disclaimer/Publisher's Note: The statements, opinions and data contained in all publications are solely those of the individual author(s) and contributor(s) and not of MDPI and/or the editor(s). MDPI and/or the editor(s) disclaim responsibility for any injury to people or property resulting from any ideas, methods, instructions or products referred to in the content.